

Estimation of Solar Energy Harvested for Autonomous Jellyfish Vehicles (AJVs)

Keyur B. Joshi, John H. Costello, and Shashank Priya

Abstract—There is significant interest in harvesting ocean energy for powering the autonomous vehicles that can conduct surveillance for long durations. In this paper, we analyze the applicability of solar cells as a power source for medusa-inspired biomimetic vehicles. Since these vehicles will be operating under ocean waters and may need to dive at various depths, a systematic investigation was conducted to determine the variation of output power as a function of depth and salinity levels. We modeled solar energy harvested by flexible amorphous solar cell coated jellyfish vehicles by considering the variables bell diameter, turbidity, depth, and fineness ratio. Low fineness ratio shapes were found to be better for solar energy powered vehicles. Study of three representative species, *Aurelia aurita* (AA), *Mastigias sp.*, and *Cyanea capillata* indicates that harvested power was proportional to bell diameter. Optimum power can be harvested by tilting the vehicle axis to face refracted sunrays. Depending on a swimming pattern, power harvested in charging mode and in propulsion mode could vary significantly. The model indicates that, under some circumstances, amorphous silicon solar cell may be a cost-effective way to power autonomous underwater vehicles (AUVs) operating in shallow-water conditions with large lateral travel distances.

Index Terms—Incidence angle, jellyfish, photovoltaic cell, salinity, turbidity, unmanned undersea vehicle.

NOMENCLATURE

I_0	Incidence radiation intensity.
I_t	Transmitted radiation intensity.
d	Depth from air–water interface.
T	Turbidity level (in ntu).
c_0, c_1, c_2	Model coefficients.
I_λ	Radiation intensity of wavelength λ .
$f(\lambda)$	Spectral distribution.

I_a	Radiation absorbed by photovoltaic cell material.
u	Extinction coefficient of water.
α	Absorption coefficient of cell material.
r	Reflection coefficient of cell material.
I_p	Harvested power intensity.
λ_g	Absorption edge.
θ_{water}	Apparent zenith angle of the sun in water.
θ_{air}	Actual zenith angle of the sun in air.
n_{water}	Refractive index of water.
n_{air}	Refractive index of air.
I_{p0}	Harvested power intensity at normal incident.
$I_{p\theta}$	Harvested power intensity at θ angle.
A	Lateral area of frustum of cone.
D	Bell diameter.
P	Power harvested.

I. BACKGROUND

UNMANNED UNDERSEA VEHICLES (UUVs) have been gaining importance for a variety of civilian and defense applications such as sea exploration, surveillance, and remote monitoring of national borders. However, conventional onboard energy available for such vehicles restricts the size, tasks, lifetime, and range of the vehicles. These vehicles tend to use more energy than the onboard batteries can supply. Thus, research has focused on enhancing the energy efficiency of these vehicles by combining more than one source of energy to satisfy the total power requirement. Solar, wave, and thermal sources of ambient energy may be available for UUVs. Rudnick *et al.* [1] have reviewed development and trends in powering underwater gliders. Some of the initial designs, such as Sound Fixing And Ranging (SOFAR) [2] in 1978, were just buoyancy controlled floats to accomplish vertical profiling at a desired location in ocean. Several different glider designs have been developed in the past decades before the development of the Autonomous Lagrangian Circulation Explorer (ALACE) and BOBBER (a category of floats made of cork-like material) [3] which introduced the concept of energy harvesting from thermoclines for propulsion. This concept was fully developed and employed in the SLOCUM (named after Joshua Slocum, first man to sail around the world) design by Webb *et al.* [4]. The SLOCUM gliders harvest propulsive energy from heat

Manuscript received August 02, 2010; accepted July 23, 2011. Date of publication September 06, 2011; date of current version October 21, 2011. This work was supported by the U.S. Office of Naval Research under Contract N00014-08-1-0654.

Associate Editor: W. Carey.

K. B. Joshi is with the Center for Intelligent Material Systems and Structures (CIMSS), Department of Mechanical Engineering, Virginia Tech, Blacksburg, VA 24061 USA (e-mail: key4josh@vt.edu).

J. H. Costello is with the Department of Biology, Providence College, Providence, RI 02918 USA (e-mail: costello@providence.edu).

S. Priya is with Center for Energy Harvesting Materials and Systems (CEHMS), Department of Mechanical Engineering and the Electronic Materials and Devices Laboratory (EMDL), Department of Material Science and Engineering, Virginia Tech, Blacksburg, VA 24061 USA (e-mail: spriya@mse.vt.edu).

Color versions of one or more of the figures in this paper are available online at <http://ieeexplore.ieee.org>.

Digital Object Identifier 10.1109/JOE.2011.2164955

flow between vehicle engines and surrounding fluids using thermal gradient existing in temperate and tropical ocean waters. The heat is used to achieve solid–liquid transformation of the working fluid resulting in buoyancy control. Additionally, a clever design of wing converts roll motion into translation. Other popular form of propulsion uses fuel cell for their efficiency and compact size, making good use of abundant cooling water. Wang *et al.* [5] proposed enhancing the proton exchange membrane fuel cell (PEMFC) efficiency by using thermal engine of SLOCUM gliders. However, it was noted that for thermal engine to work, a minimum of 10 °C temperature difference is required across ocean depths which is not available for a jellyfish vehicle. PEMFC may be an option but it suffers from poor efficiency if the heat generated in the process is not quickly removed and there are challenges in its implementation on the biomimetic vehicle.

An alternative means of energy acquisition that we explore here is the use of photovoltaic cells for conversion of the sunlight to the useful energy. A variety of cnidarian symbioses, notably corals, may meet large portions of their metabolic requirements via photosynthetic symbionts [6]. The ability of jellyfish to move to high-light environments can allow light energy to make important contributions to the jellyfish energetic demands. A variety of jellyfish species have evolved these capabilities [7], [8] and these animals provide a useful model for meeting the energetic demands of an autonomous vehicle.

II. INTRODUCTION

Villanueva *et al.* [9] have recently developed JetSum (name of the prototype) UUV inspired by jet-propelled type of jellyfish. At larger bell diameters, it is well known now that the rowers exhibit better swimming efficiencies by taking advantage from interaction between counter rotating starting and stopping vortices [10]. The breakthrough in the bio-inspired shape memory alloy composite (BISMALC) [11] actuators opened the possibility of mimicking the rower jellyfish propulsion which relies on vortex generation. The BISMALC requires large electrical power to operate in the underwater conditions. To enhance the useful life of jellyfish node based on BISMALC actuators, it is desirable to explore energy harvesting from ambient underwater environment. Nonuniversal existence of thermal gradients in shallow water makes it difficult for use of thermal engines. Solar energy is available at shallow depths in the ocean and can be used to aid the battery life and to operate low-power sensor nodes. This is the motivation behind this study and we present results on evaluation of the solar cell in ocean environment quantifying the change in its performance with ocean depth and salinity level.

Dave [12] modeled the effect of atmospheric condition on solar cell performance and numerically predicted the performance of $\text{Ga}_{1-x}\text{Al}_x\text{As}$ –GaAs solar cell. The model was based on terrestrial solar radiation at five different altitudes on average, cloud-free, mid-latitude summer conditions and incorporates absorption by CO_2 , O_2 , ozone, water vapor, and aerosols. Gonzalez [13] studied solar cell efficiency variation with atmospheric conditions, especially turbidity and humidity, using SPCTRAL2 model for both mono-crystalline as well as amorphous silicon solar cell and reported increase in conversion ef-

ficiency with increase in humidity (especially in amorphous silicon) and decrease in turbidity level.

Stoddard [14] studied distribution of solar radiation in natural waters experimentally and reported that collimated beam of solar radiation, refracted from the air–water interface redistributes and strongly influences vertical distribution of available solar radiation. This phenomenon causes maximum irradiance to occur below air–water interface and is pronounced at 22.1° angle. Muaddi *et al.* [15] presented a model for variation in solar radiation spectrum under water surface and predicted solar cell efficiency variation under water surface. They noted reduction in spectral width with depth and reported that relative efficiency of silicon solar cell increases with depth until specific point after which it reduces and becomes equal to surface efficiencies at depths of about 3.5 m. The increase in conversion efficiency was attributed to rapid reduction of long wavelength radiation and correspondingly the total available radiation energy with depth. The short wavelength radiation, including visible ranges that contribute to the cell current, does not change as rapidly with depth. Wang [16] studied the effect of turbidity and salinity on penetration of solar radiation under water and concluded that salinity has no significant effect on transmittance of solar radiation in water, but turbidity tends to reduce the available solar radiation and has more pronounced effect with increase in depth. Gottschalg [17] studied the effect of variation in solar spectrum experimentally for thin film solar cells by taking a large number of measurements over a period of 30 months covering seasonal changes and reported that amorphous silicon solar cells are most susceptible to the changes in the spectral distribution with useful fraction of light varying between +6% and –9% with maximum occurring in summer.

Research has also been done on enhancing solar cell efficiency. Chen [18] showed that the use of antireflective layer of poly (methylmetacrylate) (PMMA) on the poly-silicon solar cell improves the efficiency from 10.4% to 13.5%. Strümpel [19] presented an overview of techniques to modify solar spectrum to achieve high-efficiency solar cell by downconversion (cutting one high-energy photon into two low-energy photons), photoluminescence (shifting photons into wavelength regions better accepted by the solar cell) and up-conversion (combining low-energy photons to one high-energy photon) and better materials to achieve these effects. Custodio [20] reported improvement in the conversion efficiency achieved by reducing operating temperature of the cell by employing infrared filters. In a recent development, Yun [21] achieved increased solar cell efficiency by using full solar spectrum with a new conjugated polymer–ZnSe–PbSe nanocrystal hybrid photovoltaic cell. All these developments indicate the promise of solar cell for powering autonomous jellyfish vehicles (AJVs).

III. EXPERIMENTAL SETUP

The experimental setup, as shown in Fig. 1(a), consisted of an acrylic water tank with 200-mm nominal diameter and 1.676-m height. The solar cell and the light sensor were mounted together on a flat platform as shown in Fig. 1(b). The mounting was raised and lowered with a 200-mm nominal diameter aluminum elevator pipe attached to it along with the metal halide

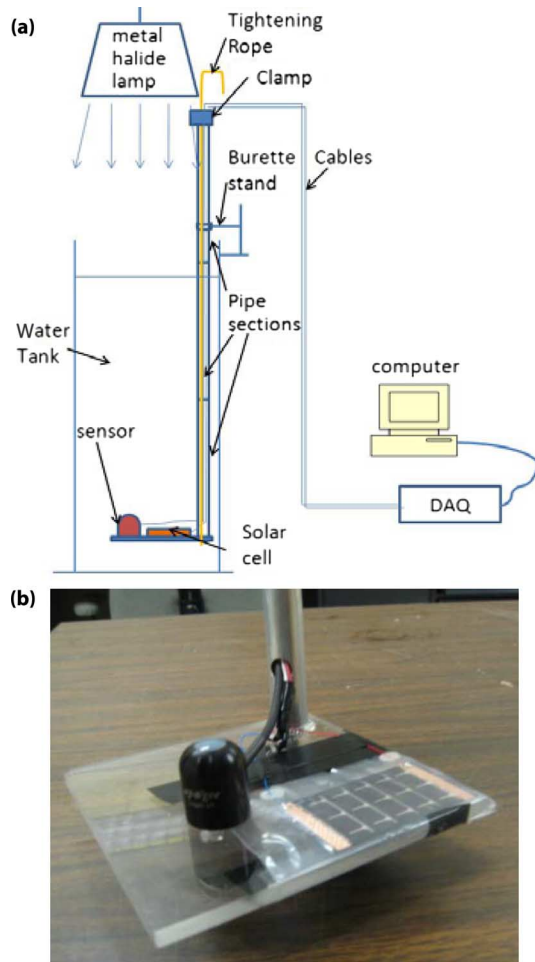


Fig. 1. (a) Schematic of the experimental setup. (b) Quantum sensor and solar cell mounted on the submersible platform.

lamp. The light source, the 400-W metal halide lamp with a concentrating reflector, was placed directly above the water tank. The water used in these experiments was tap water available in the lab. CORALIFE scientific grade marine salt was added manually to achieve different salinity levels and salinity measurements were done using an Instant Ocean hydrometer. The cables from light sensor and the solar cell were routed through the aluminum pipe to the data acquisition (DAQ) system attached to a laptop. NI-6211 DAQ card from the National Instruments (NI, Austin, TX) with 16-b analog-to-digital converters (ADCs) channels was used to obtain high resolution. The load resistor used across the cell terminal was fixed at 1 k Ω . Fig. 2(a) shows the electrical wiring diagram and Fig. 2(b) displays the LabView sample program used for the automated measurements.

A. Choice of System Components

The elevator pipe was made in segmented construction (resembling the blind man's cane) to add length as required without interfering with the metal halide lamp on top of the tank. The tension rope required to maintain platform level was routed from inside the pipe along with the electrical cables from the light sensor and the solar cell.

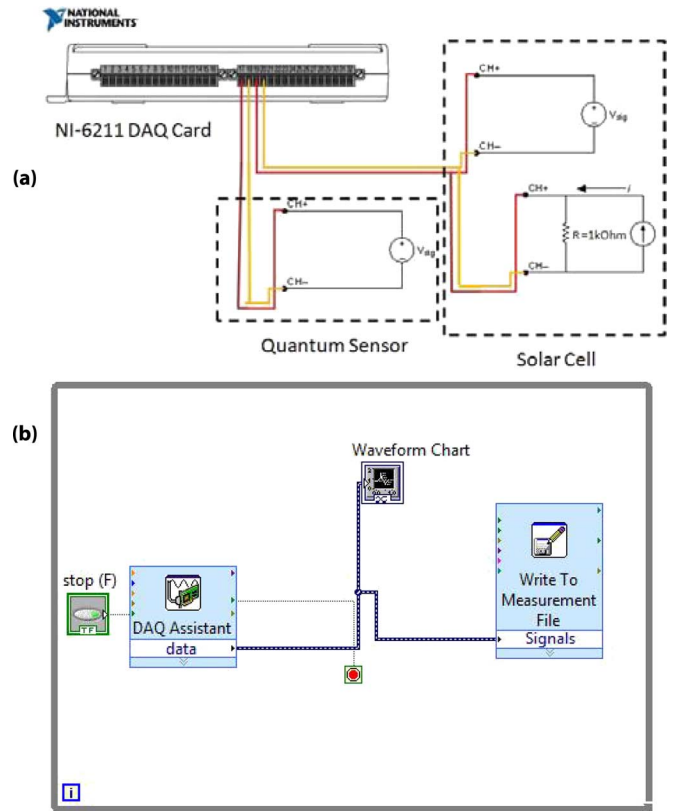


Fig. 2. (a) Wire connection to the DAQ card. (b) VI file used in the experiment.

The solar cell was waterproof and sealed with a polyethylene sheet and adhesive tapes. In the field, the solar cell is placed just below the exumbrella (the external convex surface of a jellyfish body) of the jellyfish with a thin, transparent layer of silicone on top for waterproofing. Flexible amorphous silicon solar cell films, commercially available as PowerFilm [22], were chosen to meet the flexibility requirement imposed by continuous flexing of exumbrella during propulsion of the jellyfish. It also lends itself to being coated with a thin layer of room temperature vulcanizing (RTV) silicone rubber for weather protection in underwater environment without a significant drop in performance. The particular cell used for the test, SP3-37 (5×3.5 cm²), is rated to provide 22-mA output current at 3 V.

SQ-110 quantum sensor from Apogee Instruments, Logan, UT [23] has the ability to measure the radiation intensities in the active spectral range of amorphous silicon and is suitable for use in underwater environment. Fig. 3(a) shows the spectral response of the sensor in active range which also encompasses full spectrum of the metal halide lamp shown in Fig. 3(b). The sensor measurement was calibrated for photosynthetic photon flux (PPF) measurement, which can be converted into corresponding radiation intensity by multiplying the value with energy required to generate a photon at average wavelength and dividing by the active sensor area. The light source, Cayman Sun 400-W HQI System with a metal halide bulb, has the capability of simulating 14-K temperature. Thus, this system was chosen for its capability of simulating full sun spectrum up to 6-m depth in water [24].

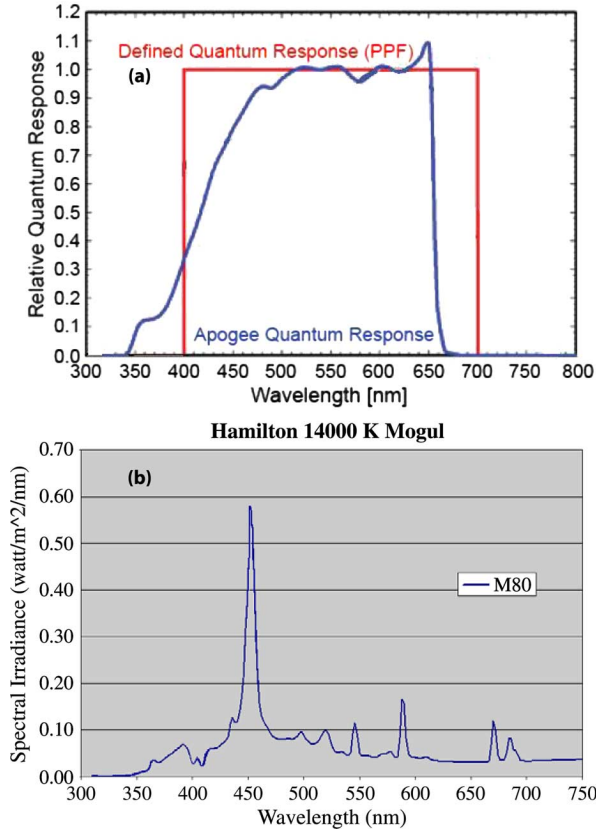


Fig. 3. (a) Spectral response of the quantum sensor SQ-110 [23]. (b) Spectral plot of the metal halide lamp used with electronic ballast M80 [25].

IV. EXPERIMENTAL RESULTS

Fig. 4(a)–(e) illustrates the experimental results on variation of voltage, current, available radiation intensity, harvested power intensity, and efficiency with depth. Interestingly, the efficiency peaks at depth of ~ 40 cm to about 28%. This observation agrees with the prior result reported by Muaddi [15]. The reason for apparent increase in efficiency is related to faster rate of decrease in available radiation density with depth due to absorption of longer wavelength radiation compared to reduction in shortwave radiation. Since amorphous silicon solar cell utilizes only shortwave radiation for conversion into electrical energy, the conversion efficiency increases. After a certain depth, reduction in shortwave radiation becomes more significant and efficiency begins to drop. The voltage and current plots exhibit maximum at certain depth from the air–water interface and then show a continuing decreasing trend. The variation with salinity did not show any conclusive trend and is within the error bar of the experiment. Wang [16] conducted an experiment with salt concentration as high as 25% and showed that salt concentration does not have any noticeable effect on radiation energy transmission. Our experiments are in agreement with his results. The error bar was determined based on three sets of experiments with seven different salinity levels at each depth [0, 6, 15, 21, 31, 33, and 37 part per thousand (PPT)] of marine grade salt.

Authorized licensed use limited to: b-on: Instituto Politecnico de Tomar. Downloaded on April 19, 2024 at 18:30:58 UTC from IEEE Xplore. Restrictions apply.

V. MODEL FOR UNDERWATER ENERGY HARVESTING USING SOLAR CELL

A. The effect of Turbidity on Transmission of Solar Radiation

Ocean turbidity is a measure of haziness of the ocean waters and is computed in one of the popular units: the nephelometric turbidity unit (ntu). Ocean turbidity changes with atmospheric conditions such as hurricane, storm, rain, depth of the ocean floor, distance from shore, mouth of a river, suspended organic matters, etc. Typical ocean turbidity is found to be in the range of 1–7 ntu. Wang [16] studied the effect of turbidity on the transmission of solar radiation in underwater environment and presented experimental data for the transmission coefficient in the turbidity range of 1–4.5 ntu at depths up to 1.34 m. We developed a mathematical model to fit his experimental data. An individual curve at a particular depth follows a quadratic function, for which, coefficients c_0 , c_1 , and c_2 were found to obtain the least square fit. These coefficients varied linearly with depth. The transmission coefficient is given by

$$\frac{I_t}{I_0} = c_0(d) - c_1(d)T + c_2(d)T^2 \quad (1)$$

where I_t is the transmitted radiation intensity, I_0 is the incidence radiation intensity, d is the depth from the air–water interface, T is the turbidity level, and c_0 , c_1 , c_2 are coefficients that vary with depth. The variation laws for these coefficients are given by

$$c_0(d) = 1.00041 + 0.060862d \quad (2)$$

$$c_1(d) = 0.000159442 + 0.202067d \quad (3)$$

$$c_2(d) = 0.00025378 + 0.013629d. \quad (4)$$

Fig. 5 illustrates the mathematical model fitted to the experimental data presented by Wang [16]. This mathematical modeling extends the transmission estimation to turbidity and depth levels not covered by the experimental data and allows us to predict the behavior over a wider range.

B. Variation of Solar Spectrum and Solar Cell Response With Underwater Depth

Our experiment confirmed the trends predicted by numerical model of Muaddi [15]. Hence we take advantage of their numerical data to predict the spectrum variation and solar cell spectral response at depths as large as 100 m. The solar spectrum gets modified with depth from air–water interface. Muaddi's numerical model [15] predicts underwater solar spectrum with variation in depth. This model was built by considering atmospheric absorption bands from spectrum as received at the top of the atmosphere and reduces the radiation intensities to 70% to arrive at an incident radiation spectrum on the water surface. The radiation energy available is given by

$$I_\lambda(x) = \int_{\lambda_0} I_t e^{-u(\lambda)x} f(\lambda) d\lambda \quad (5)$$

where x is depth from water surface, λ is the wavelength of the radiation, I_λ is a transmitted intensity at x meters from water surface, I_t is a transmitted intensity at water surface, $u(\lambda)$ is the extinction coefficient of water, and $f(\lambda)$ is the spectral distribution function. This model does not include the effect of water

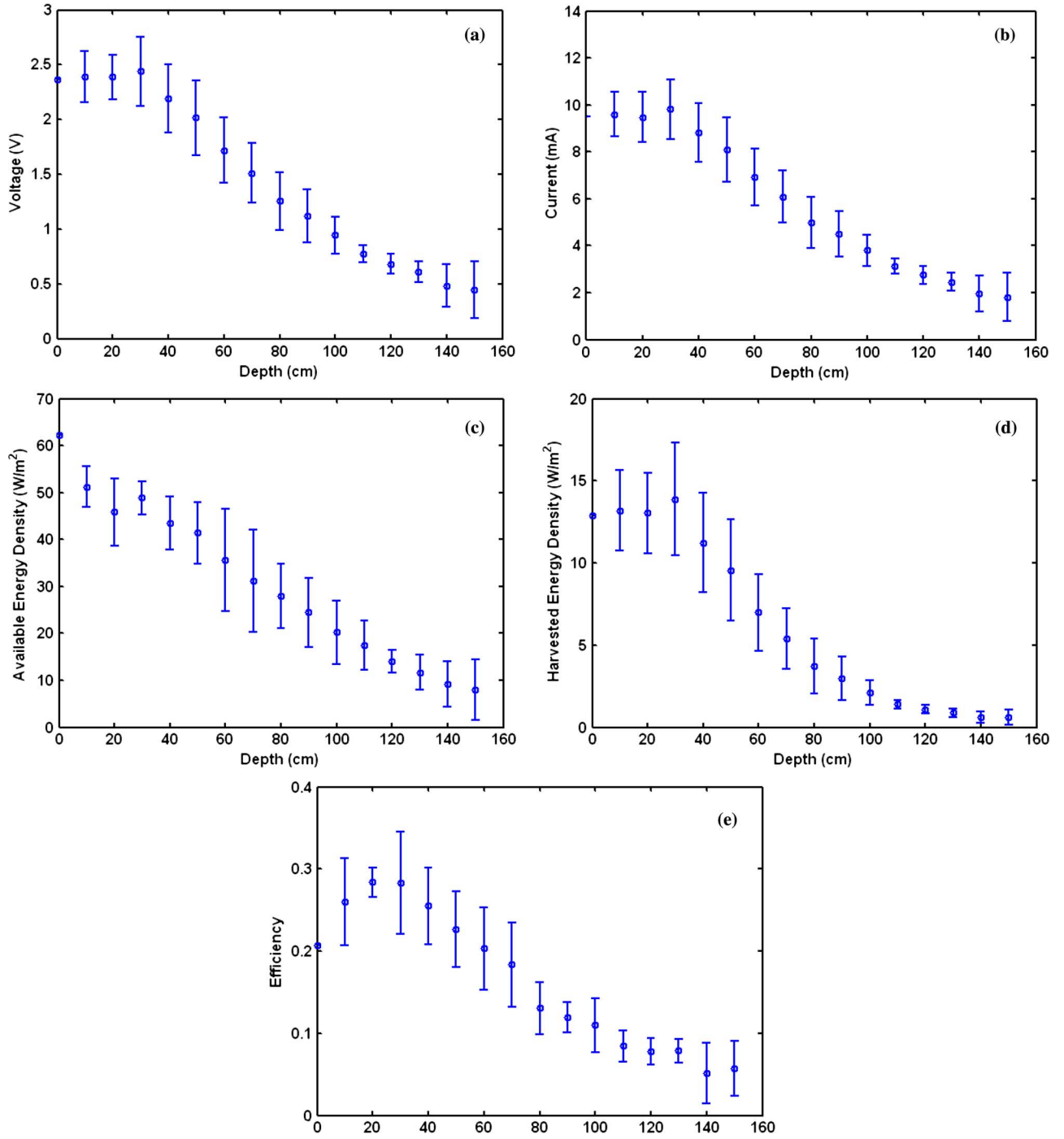


Fig. 4. Variation with depth in (a) voltage, (b) current, (c) available power density, (d) harvested energy density, and (e) conversion efficiency of the solar cell. The error bar was determined from 21 data points for each depth level.

turbidity. To include the effect of turbidity, we use the model developed in (1)–(4) for calculation of the transmitted radiation energy with respect to depth and turbidity. The transmitted energy upon incidence on solar cell is reflected and absorbed which is described by

$$I_a(\lambda) = \int_0^{\infty} I_{\lambda}(x) [1 - r(\lambda)] [1 - e^{-\alpha(\lambda)x}] d\lambda \quad (6)$$

where $I_{\lambda}(x)$ is an incident energy intensity at x meters of depth, $r(\lambda)$ is the reflection coefficient of the solar cell material, and

$\alpha(\lambda)$ is the absorption coefficient of the solar cell material. From this absorbed energy I_a , the solar cell converts a fraction of energy into useful electrical energy according to

$$I_p = \int_0^{\lambda_g} I_a(\lambda) d\lambda \quad (7)$$

where $\lambda_g = hc/E_g$ is the absorption edge, h is Planck's constant, c is the velocity of light, and E_g is the band gap energy for the solar cell material.

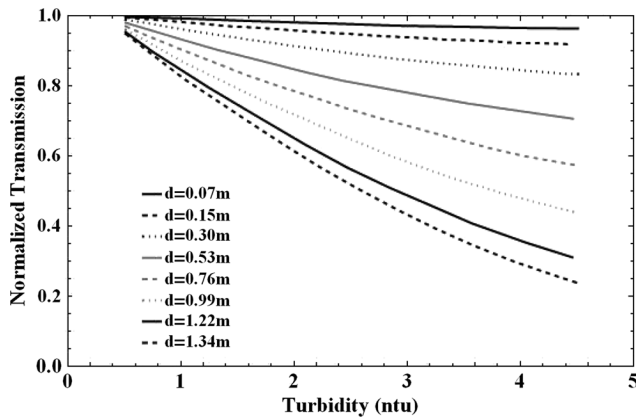


Fig. 5. Mathematical model for variation of normalized transmission with turbidity and depth using data from Wang [15]. (Based on data from J. Wang, S. Yagoobi, "Effects of turbidity and salt concentration levels on penetration of solar radiation under water," *Solar Energy*, vol. 52, no. 5, pp. 429–438, 1994; printed with permission from Elsevier.)

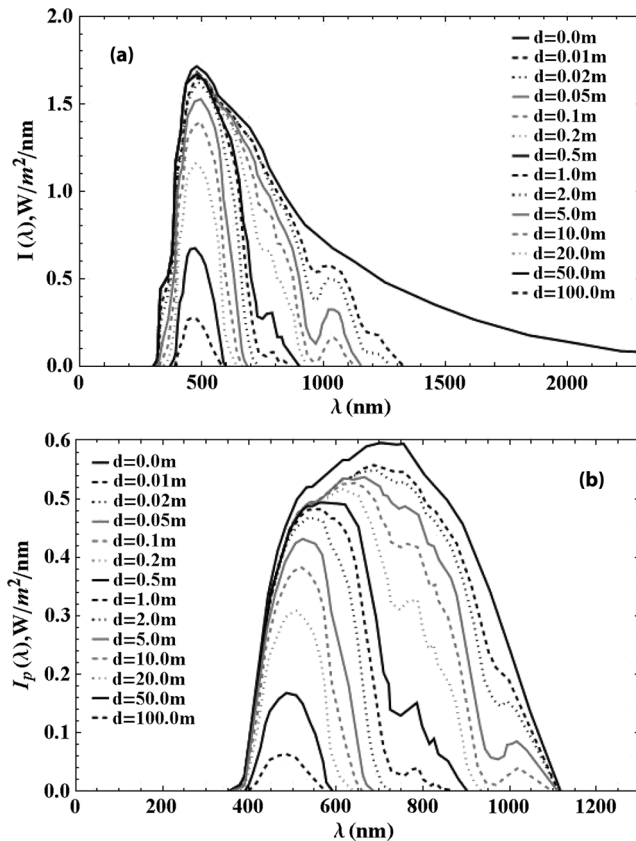


Fig. 6. (a) Solar spectral variation with depth in water [7]. (Reprinted from J. A. Muaddi, M. A. Jamal, "Spectral response and efficiency of a silicon solar cell below water surface," *Solar Energy*, vol. 49, no. 1, pp. 29–33, 1992, with permission from Elsevier.) (b) Single-crystal silicon cell spectral response with depth in water [7].

The solar spectral variation with depth is depicted in Fig. 6(a) and the corresponding spectral response of a single-crystal silicon solar cell is shown in Fig. 6(b). The data in this figure were generated from a single-crystal solar cell and cannot readily be extended to an amorphous silicon solar cell. We used the spectral response of single-crystal silicon and amorphous

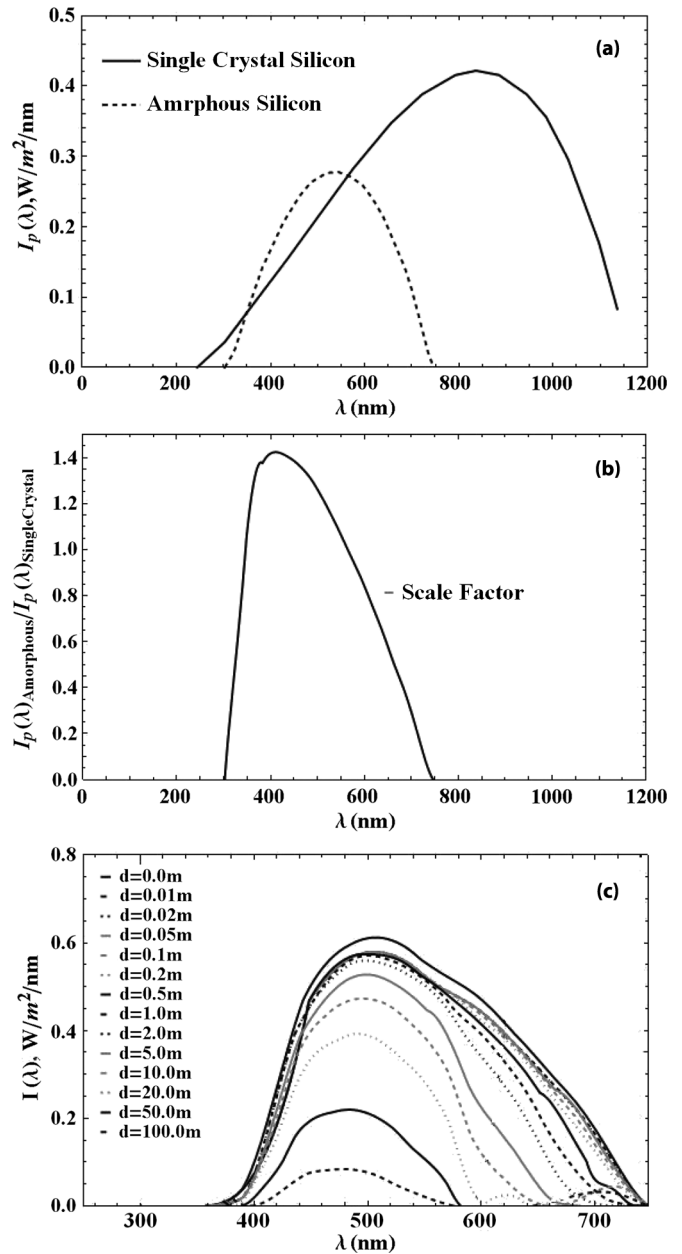


Fig. 7. (a) Comparison of spectral response of single-crystal silicon with amorphous silicon [13]. (Reprinted from M. C. Gonzalez, J. J. Carol, "Solar cells efficiency variations with varying atmospheric conditions," *Solar Energy*, vol. 53, no. 5, pp. 395–402, 1994, with permission from Elsevier.) (b) Factor applied to scale the single-crystal silicon spectral response with that of an amorphous silicon. (c) Spectral response of the amorphous silicon cell obtained after scaling.

silicon solar cells from [13] as shown in Fig. 7(a) to scale the single-crystal spectral response given by Fig. 6(b). The scaling factor is shown in Fig. 7(b). It should be noted from Fig. 6(a) that the solar spectrum shrinks down with increase in depth to 400–600-nm range. For the most part of this range (350–550 nm), the scaling factor is greater than 1. This result shows that the amorphous silicon solar cell may be better for harvesting solar energy in the underwater environment in comparison to its single-crystal counterpart. This result also provides a relative cost advantage due to low-cost manufacturing of the amorphous silicon cell. After scaling, the spectral response for an amorphous silicon cell is as shown in Fig. 7(c).

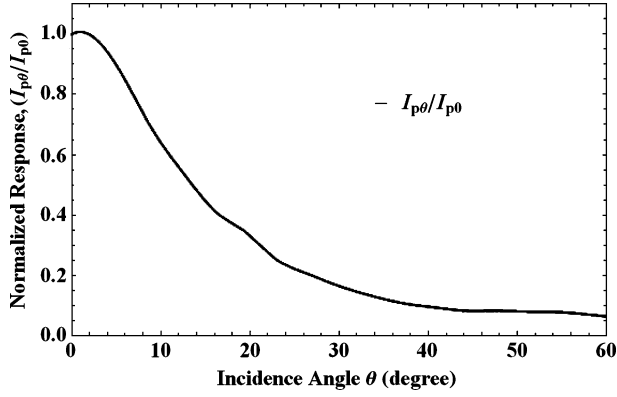


Fig. 8. The effect of the incidence angle on harvested solar energy.

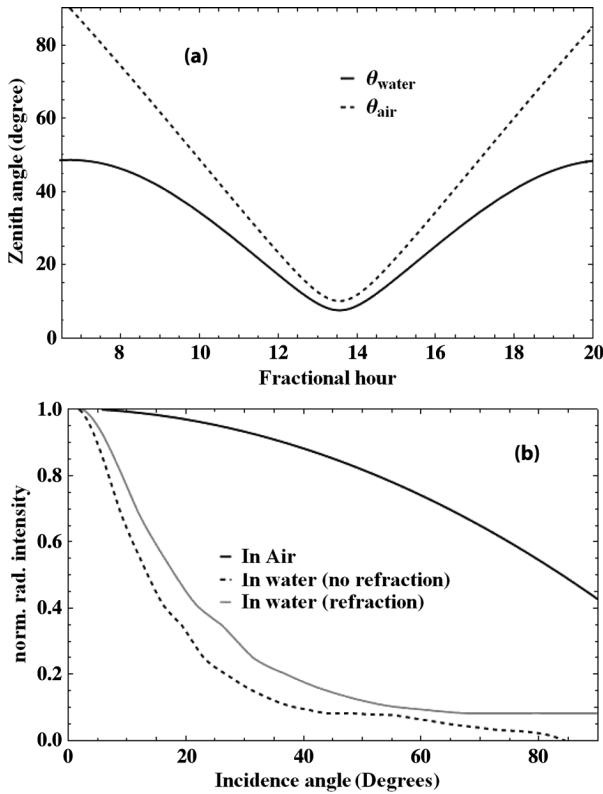
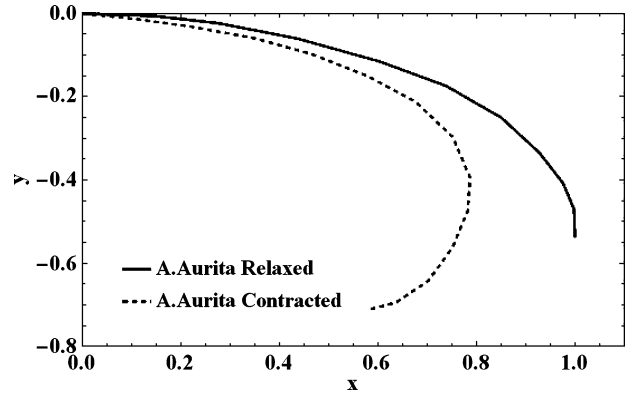


Fig. 9. (a) Apparent zenith angle of sun in water. (b) The effect of the incidence angle in presence of refraction.

C. The effect of Incidence Angle

For estimation of solar power harvested by covering exumbrella of jellyfish vehicle with solar cell, we need to take into account the effect of incidence angle as solar radiation is received by the animal at different incidence angle along the length of its bell. Stoddard and Incropera [14] studied the response of incidence angle in underwater environment in actual sun. We modified their result to calculate the response of solar cell with respect to the angle made with the incidence beam instead of the air–water interface by subtracting the apparent zenith angle of the sun from the data. We used a third-order interpolation function to obtain a continuous response function of normalized radiation intensity as a function of incidence angle as shown in Fig. 8. The model extrapolates incidence angles beyond the range of available experimental data.

Authorized licensed use limited to: b-on: Instituto Politecnico de Tomar. Downloaded on April 19, 2024 at 18:30:58 UTC from IEEE Xplore. Restrictions apply.

Fig. 10. Normalized *Aurelia aurita* exumbrella profile [26].

Due to refraction of the solar beam, the actual incidence angle onto the underwater surface parallel to air–water interface is smaller than the actual zenith angle of the sun above the interface, which is advantageous for harvesting in underwater environment. Using Snell's law

$$\frac{\sin(\theta_{\text{water}})}{\sin(\theta_{\text{air}})} = \frac{n_{\text{air}}}{n_{\text{water}}} = \frac{3}{4} \quad (8)$$

where θ_{water} is the apparent zenith angle in water, θ_{air} is the actual zenith angle of the sun, n_{air} is the refractive index of air, and n_{water} is the refractive index of water.

This is advantageous as apparent zenith in water can only be 48.6° (critical angle for total internal reflection). As an illustration, Fig. 9(a) plots the actual sun zenith in air and the apparent zenith in water near a possible deployment location in Florida ($34^\circ 26' \text{ N}$, $84^\circ 17' \text{ W}$) on May 21, 2010. However, this advantage does not overcome the sharp reduction in radiation intensity with incident angle in water compared to that in air as illustrated by Fig. 9(b).

D. Estimation of Power Harvested for Jellyfish Node

We combine all the above mentioned effects to estimate the power that can be harvested from the jellyfish node if its entire top surface is covered with the flexible amorphous silicon solar cell. We used the jellyfish profile of *Aurelia aurita* as shown in Fig. 10 [26] and scaled it parametrically using the bell diameter (D) in relaxed condition.

The parameters considered in the calculation are depth d (distance of jellyfish top from the water surface), jellyfish bell diameter D , and turbidity level T . Consider a small strip of frustum of a cone at x as shown in Fig. 11.

Its lateral area can be given by

$$A(D, x) = \pi D^2 (x + (x + dx)) \sqrt{dx^2 + dz^2(x, dx)}. \quad (9)$$

Assuming that jellyfish is facing directly up, and sun is at zenith directly above the jellyfish, the incidence angle is given by

$$\theta = \tan^{-1} \left(\frac{dz}{dx} \right). \quad (10)$$

The power harvested from this frustum of a cone can be calculated by multiplying the integrated scaled spectral response of

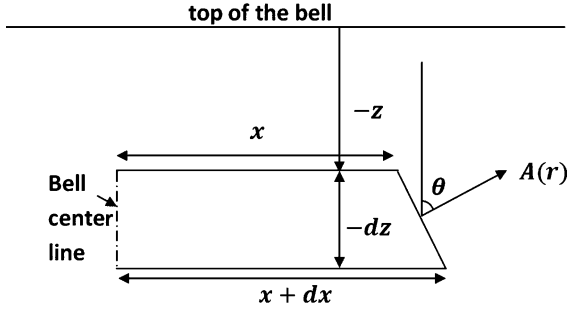


Fig. 11. Small frustum of a cone of height dz at position x .

an amorphous silicon cell with lateral area, transmission coefficient, and relative intensity at the incidence angle of the area. This is represented by

$$\begin{aligned}
 P(d, T, D, x) &= A(D, x) \left[c_0 \left(d - z - \frac{dz}{2} \right) - c_1 \left(d - z - \frac{dz}{2} \right) T \right. \\
 &\quad \left. + c_2 \left(d - z - \frac{dz}{2} \right) T^2 \right] \\
 &\times \left[\int_{\lambda} I_{p\lambda(sc)} \left(d - z + \frac{dz}{2} \right) \left(\frac{I_{p\lambda(as)}}{I_{p\lambda(sc)}} \right) d\lambda \right] \\
 &\times \left(\frac{I_{p\theta}}{I_{p0}} \right). \quad (11)
 \end{aligned}$$

The total power harvested by the vehicle is calculated by integrating (11) over radius

$$P(d, T, D) = \int_0^{\frac{D}{2}} P(d, T, D, x) dx. \quad (12)$$

VI. PARAMETRIC STUDY OF POWER ESTIMATION

A. The effect of Fineness Ratio

Jellyfish shape can be approximated by a semi-ellipsoid. Fineness ratio (h/D), defined as ratio of jellyfish height to the bell diameter, is an important parameter for describing jellyfish shape. It governs the swimming pattern preferred by jellyfish. High fineness ratio jellyfish are jetters whereas low fineness ratio oblate jellyfishes select the rowing mode of swimming. Besides this, fineness ratio also affects solar energy harvested by the model presented here. Increase in this parameter leads to increase in the area of the exumbrellar surface (tends to increase the harvested energy) and increase in the inclination angle of the area at any radial location x other than the center ($x = 0$) according to (16) (tends to decrease the harvested energy). For a constant bell diameter, equation of an ellipse with a major axis of one unit can be written as

$$x^2 + \left(\frac{h}{2D} \right)^2 y^2 = 1. \quad (13)$$

Thus

$$y = \frac{h}{2D} \sqrt{1 - x^2} \quad (14)$$

$$\frac{dy}{dx} = - \frac{\left(0.5 \frac{h}{d} \right) x}{\sqrt{1 - x^2}}. \quad (15)$$

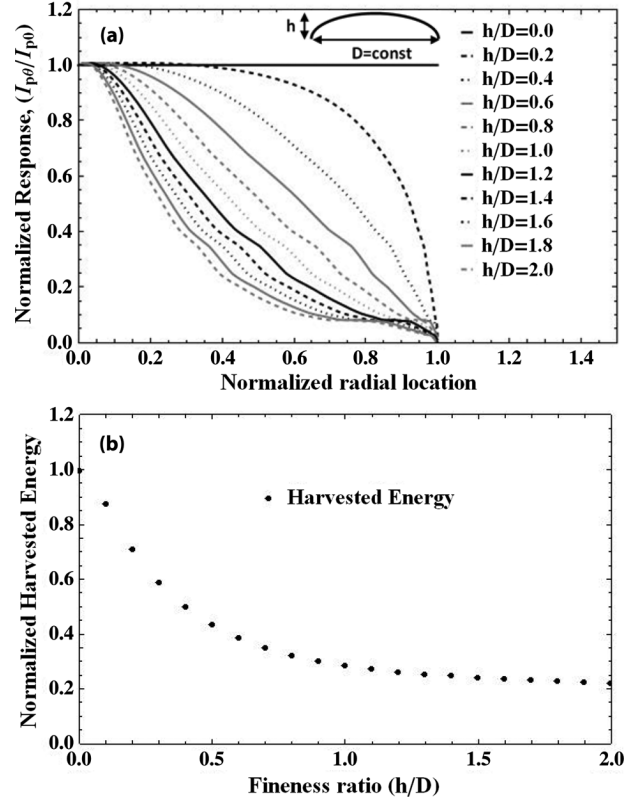


Fig. 12. (a) The effect of only the incidence angle on harvested energy. (b) The effect of the increased area and the incidence angle on total harvested energy as a result of the increasing fineness ratio.

The inclination angle at any location on the semi-ellipsoid is given as

$$\theta(x) = \tan^{-1} \left(- \frac{\left(0.5 \frac{h}{d} \right) x}{\sqrt{1 - x^2}} \right) \quad (16)$$

where $0.5(h/d)$ is a semiminor axis of the ellipsoid and x is a normalized radial location.

Increased incidence angle reduces harvested energy density as shown in Fig. 12(a).

Fig. 12(b) illustrates reduction in total energy harvested considering both effects of increasing area by increased fineness ratio and incident angle.

This model is very useful in studying parametric variation in power harvested with change in depth, turbidity, and bell diameter. We present here a comparison between three representative jellyfish species, namely, *Aurelia aurita* (Fig. 10), *Mastigias sp.* [Fig. 13(a)], and *Cyanea capillata* [Fig. 13(b)]. *A. aurita* and *C. capillata* are sennaeostome medusae and *Mastigias sp.* is a representative of the diverse rhizostome scyphozoan lineage. The selection of these three species is based on their spread in the common waters of interest.

For an illustrative case of $d = 1$ m, $T = 1$ ntu, and $D = 0.164$ m, the power generated by these three species in relaxed and contracted conditions is tabulated in Table I and also compared in Fig. 13(c).

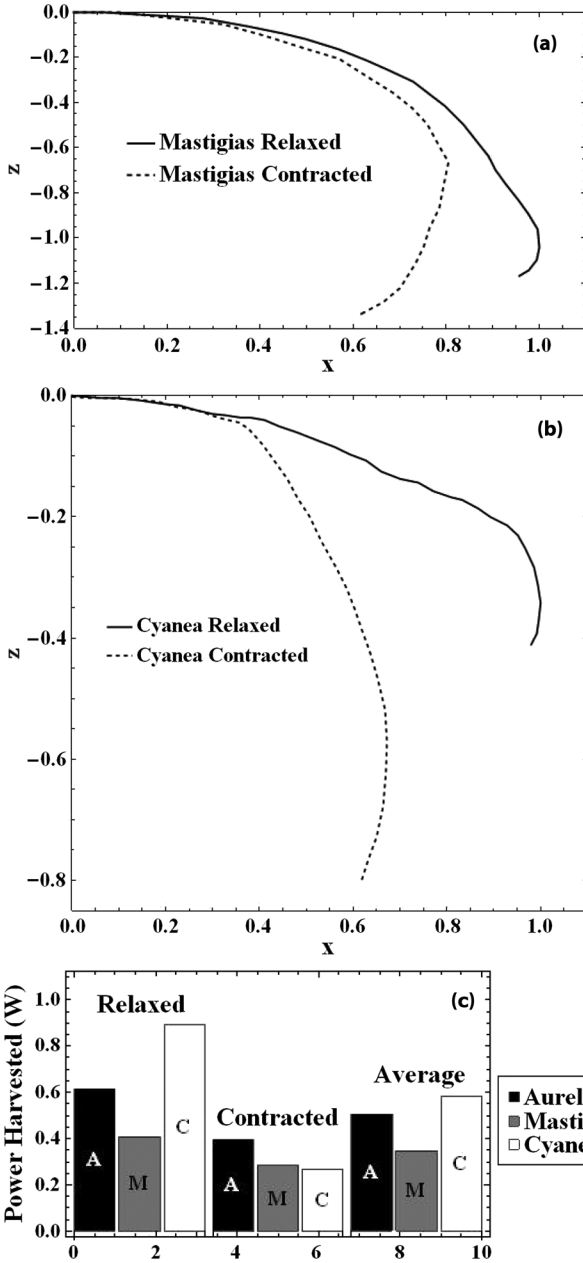


Fig. 13. (a) *Mastigias sp.* exumbrella profile (courtesy: Dr. J. H. Costello). (b) *Cyanea capillata* exumbrella profile [27]. (c) Comparison of power harvested by jellyfish species *A. aurita*, *Mastigias sp.*, and *C. capillata* in a relaxed condition, a contracted condition, and an average power over the cycle.

Fig. 14(a)–(f) illustrates the variation in the estimated power with bell diameter, ocean turbidity, and depth in water, respectively, for the three jellyfish species under relaxed and contracted conditions.

VII. GENERALIZED MODEL

The simplified model presented in an earlier section is useful for studying the effect of various parameters, but in real field application, we need to account for power harvesting capability with general orientation of AJV with respect to sun.

Consider the geometric setup as depicted in Fig. 15. The base coordinate system (B) was assumed to be located directly above the AJV top-center. The \vec{Z}_b axis was in depth direction,

TABLE I
COMPARISON OF POWER HARVESTED BY DIFFERENT SPECIES

Species	Power Harvested (W)		
	Relaxed condition	Contracted condition	Average
<i>A. aurita</i>	0.613	0.395	0.504
<i>Mastigias sp.</i>	0.409	0.283	0.346
<i>C. capillata</i>	0.892	0.269	0.581

and \vec{X}_b and \vec{Y}_b axes were taken to be parallel to longitude and latitude. AJV coordinate system (J) was fixed such that \vec{Z}_J becomes AJV central axis pointing upward. \vec{X}_J and \vec{Y}_J axes can be placed arbitrarily following the right-hand rule. At point p on the AJV surface, normal area vector \vec{A} is shown by a black arrow and the incremental area is shown by a black patch. The refracted sunray direction is shown by vector $\vec{S} = (l_s, m_s, n_s)$. Direction cosines of \vec{X}_J , \vec{Y}_J , and \vec{Z}_J in system B are $(l1, m1, n1)$, $(l2, m2, n2)$, and $(l3, m3, n3)$. We can define a rotational transform by

$$R = \text{Transpose} \begin{bmatrix} l1 & l2 & l3 \\ m1 & m2 & m3 \\ n1 & n2 & n3 \end{bmatrix} = \begin{bmatrix} l1 & m1 & n1 \\ l2 & m2 & n2 \\ l3 & m3 & n3 \end{bmatrix}. \quad (17)$$

Multiplying the AJV geometry by the transform R would map the points and vectors from the coordinate system J to that in the coordinate system B . The available 2-D profiles shown in Figs. 10 and 13(a) and (b) can be used to define any point in system J as

$$\vec{p}_J = (X(s) \cos \Gamma, X(s) \sin \Gamma, Z(s)) \quad (18)$$

where $X(s)$ and $Z(s)$ are exumbrella profile coordinates as a function of profile length, s and Γ are an angle of the 3-D point from the \vec{X}_J axis. The area vector \vec{A}_J has the magnitude given as

$$|\vec{A}_J| = X(s) \left(\frac{D}{2} \right) d\Gamma ds \left(\frac{D}{2} \right) \quad (19)$$

and

$$\vec{A}_J = |\vec{A}_J|(-\sin \theta, 0, \cos \theta) \quad (20)$$

where $\theta = \arctan[X'(s), Z'(s)]$. In the base coordinate system, the point and area vectors are given by

$$\vec{p}_b = R \cdot \vec{p}_J \quad (21)$$

$$\vec{A}_b = R \cdot \vec{A}_J. \quad (22)$$

The incidence angle for the incremental area is given by

$$i = \cos^{-1} \frac{\vec{A}_b \cdot \vec{S}}{|\vec{A}_b| |\vec{S}|} \quad (23)$$

where \vec{S} are sunrays after refraction in the air–water interface located in the base coordinate system. We can obtain \vec{S} if we know the sunrays' orientation in air $\vec{S}_{\text{air}} = (l_a, m_a, n_a)$ by

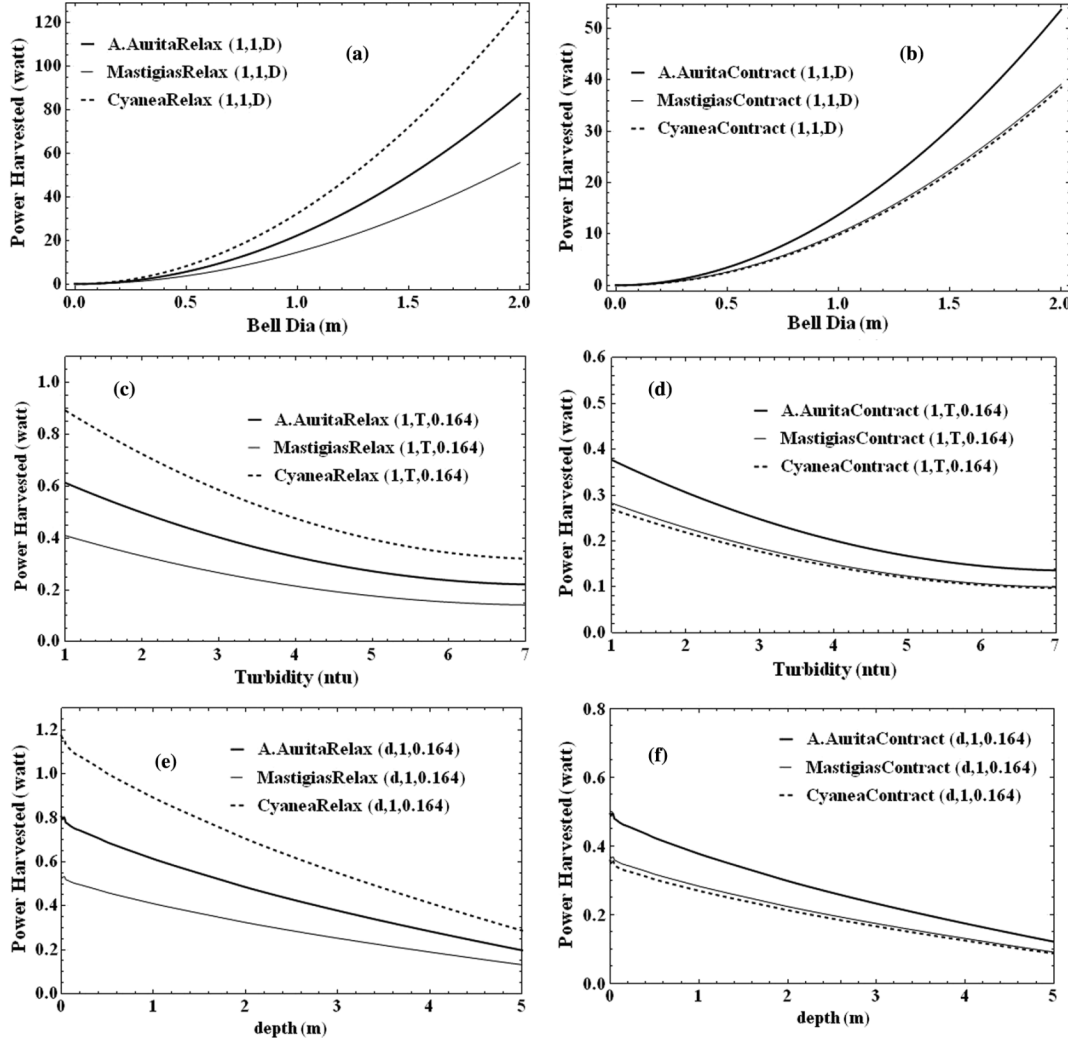


Fig. 14. Harvested power variation with jellyfish bell diameter in a (a) relaxed and (b) contracted condition. Harvested power variation with turbidity of ocean water in a (c) relaxed and (d) contracted condition. Harvested power variation with depth from the ocean surface in a (e) relaxed and (f) contracted condition.

applying axis-angle rotation transformation along $\vec{S}_{\text{air}} \times \vec{Z}_b$ axis, which is perpendicular to the plane of refraction, by angle $\theta_{\text{air}} - \theta_{\text{water}} = \cos^{-1} n_a - \sin^{-1}(\sin(\cos^{-1} n_a)(n_{\text{air}}/n_{\text{water}}))$. Depth of the point is given as

$$z_b = \vec{p}_b \cdot \vec{Z}_b. \quad (24)$$

The total power calculated is given as

$$\begin{aligned} P(d, T, D) &= \int_0^l \int_0^{2\pi} X(s) \left(\frac{D}{2}\right)^2 \\ &\times \left[c_0 \left(d - \left(z_b + \frac{dz_b}{2} \right) \right) - c_1 \left(d - \left(z_b + \frac{dz_b}{2} \right) \right) T \right. \\ &\quad \left. + c_2 \left(d - \left(z_b + \frac{dz_b}{2} \right) \right) T^2 \right] \\ &\times \left[\int_{\lambda} I_{p\lambda(sc)} \left(d - \left(z_b + \frac{dz_b}{2} \right) \right) \left(\frac{I_{p\lambda(as)}}{I_{p\lambda(sc)}} \right) d\lambda \right] \\ &\times \left(\frac{I_{p\theta}}{I_{p0}} \right) d\Gamma ds. \end{aligned} \quad (25)$$

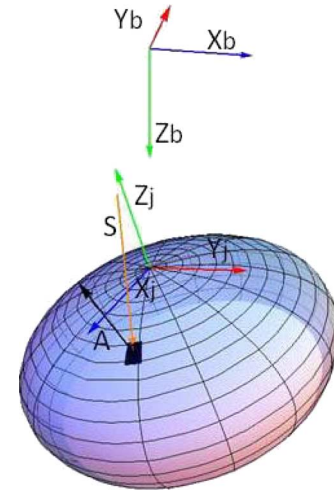


Fig. 15. Generalization of the solar energy harvesting model considering general orientation of AJV and sun.

With this model, we can study the effect of inclination of sunrays and orientation of AJV on the total harvested power.

Fig. 16(a) and (b) illustrates the effect of vehicle tilt and inclination of refracted sunrays on the harvested power. Fig. 16(c)

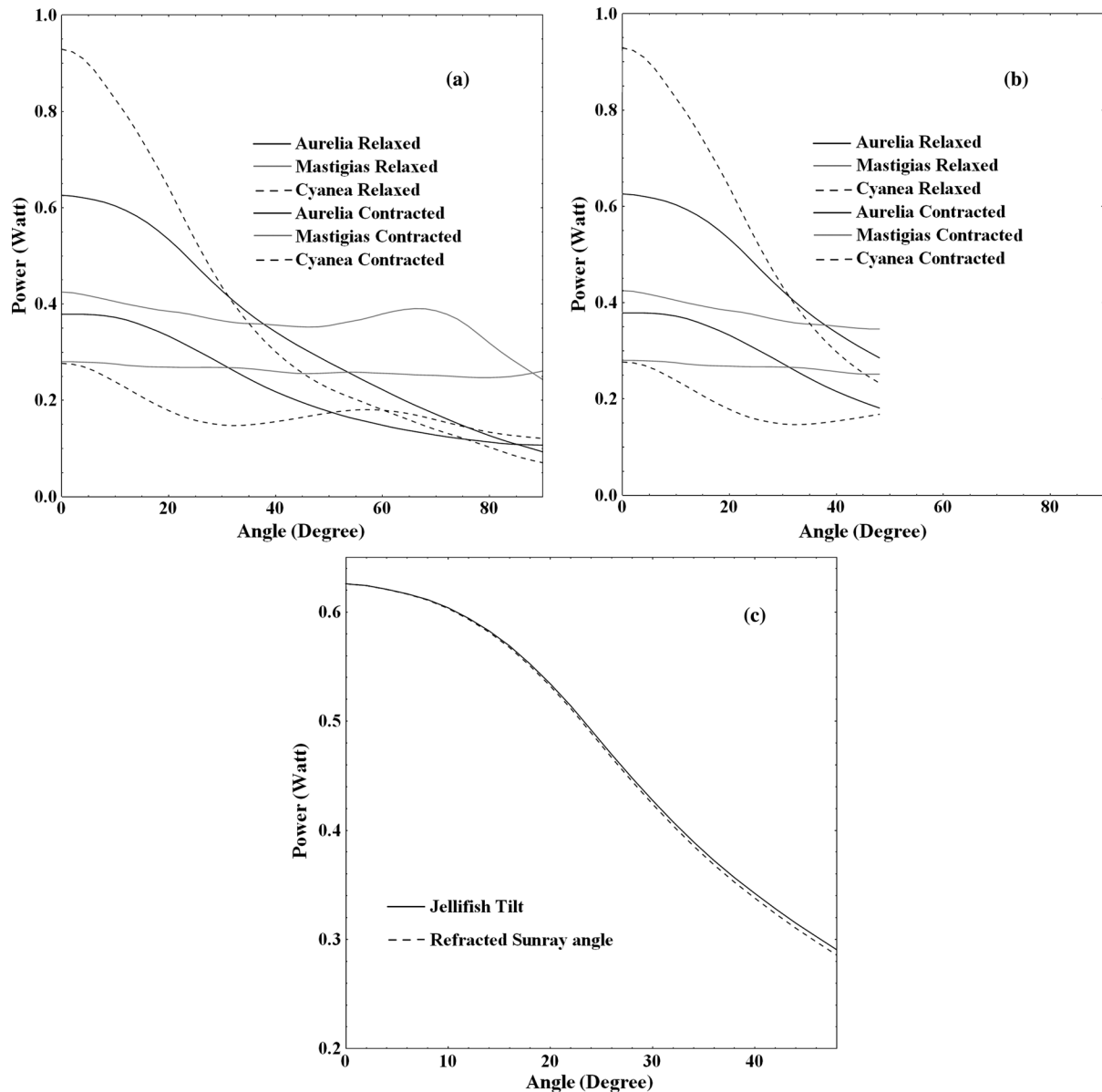


Fig. 16. (a) The effect of AJV tilting along its axis on harvested power. (b) The effect of refracted sunray inclination on harvested power. (c) Comparison of the effect of vehicle tilt and the inclination of refracted sunrays for the *Aurelia aurita* relaxed profile.

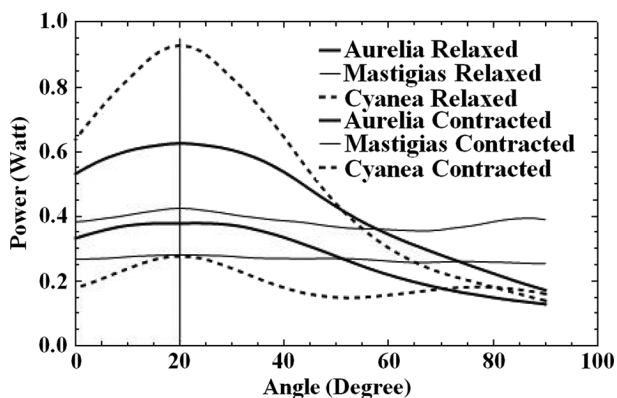


Fig. 17. Optimizing the power harvested by orienting AJV axis towards the refracted sunrays.

compares both these effect for the *Aurelia aurita* relaxed condition. The trend is almost identical, with small difference re-

lated to change in depth of the different point on AJV surface as it tilts on its axis. This effect is obviously absent in the other case resulting in small difference. This difference may increase as the depth decreases, however for practical purposes, we can consider it negligible. This result opens up an opportunity to optimize the power harvested by tilting the vehicle axis such that it is always in the direction of refracted sunrays. Fig. 17 shows that if refracted sunrays are striking at 20° angle, the maximum power can be obtained by tilting the vehicle axis towards the refracted sunrays.

VIII. CONCLUSION

In this paper, we investigated the solar energy as a potential source for powering AJV. It was experimentally confirmed that salinity has no significant effect on the performance of a solar cell but harvested power decreases with depth. The available power initially decreases with depth, mainly due to absorption and reflection of long wave radiation and solar spec-

trum shrinks and shifts towards short wavelength range around 400–600-nm range which is advantageous for amorphous silicon. Reduction in long wave radiation also results in increase in conversion efficiency with depth (~30–40% at depth 0.2 m), before reaching the peak at 0.2 m. Beyond this depth, the efficiency shows a decreasing trend. Transmission of solar radiation decreases rapidly with depth and with increasing turbidity. The variation was found to be quadratic in turbidity and the coefficients of quadratic relation were linear functions of depth. The performance of solar cells was found to be severely affected by the angle of incidence of the sun radiation. The variation can be represented by a bell-shaped curve. Higher refractive index of water was advantageous for undersea solar energy harvesting as the apparent zenith angle of sun is lower than that in the air. This helps to reduce the variation in incidence angle over the entire day. However, the reduction in radiation intensity in water is much sharper in comparison to that in air which overcomes this advantage.

An analytical model was developed to estimate the power harvested from AJV using spectral response of single-crystal silicon cell with depth and applying a scaling factor to obtain the amorphous silicon cell response. Incident radiation was modified by using transmissibility information with depth and turbidity. Total power was estimated by integrating the real power density over an incidence angle and a diameter. The model suggested monotonic reduction in harvested power with increase in fineness ratio (aspect ratio) of AJV.

It was found that in a relaxed state, *Cyanea capillata* harvests the maximum power followed by *Aurelia aurita* and *Mastigias sp.*, for the same bell diameter. However, *Cyanea capillata* harvests the least power in contracted state due to an increased inclination angle over the majority of its bell area. *Aurelia aurita* harvests the maximum power in the contracted state. Comparison of average power harvested suggests that *Cyanea capillata* would be able to harvest the maximum average power for a continuous operation. The parametric study suggested that variation in power harvested is a parabolic function of the AJV bell diameter. For a diameter of 2 m with turbidity of 1 ntu and depth of 1 m, we can expect power in excess of 85, 55, and 125 W, respectively, from AJV mimicking *Aurelia aurita*, *Mastigias sp.*, and *Cyanea capillata* profiles in a relaxed condition. These are promising values for developing a surveillance vehicle that can be deployed in the ocean. AJVs can also charge their onboard batteries by staying on the surface for their intermittent propulsive needs. With the increase in turbidity from 1 to 7, a quadratic decrement was observed that caused reduction in power harvested by more than 60%. With depth, power harvested increases slightly due to an increased efficiency and after that shows a monotonous decreasing trend. At 5-m depth, the power available was reduced by 75%.

A generalized model enabled power harvesting estimates in any field condition. It also suggests the advantage of tilting of the vehicle to face refracted sunrays. *Cyanea capillata* suffers the most if the refracted sunrays and the AJV axis are not aligned. *Mastigias sp.* is least affected, giving almost constant power output at all inclinations. *Aurelia aurita* shows an intermediate behavior. Thus, *Mastigias sp.* has the optimum shape for AJVs required to achieve the effective lateral motion. We

expect this work to provide a guideline for developing not only AJVs but also other forms of AUVs.

REFERENCES

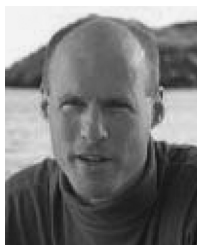
- [1] D. L. Rudnick, R. E. Davis, C. C. Ericson, D. M. Frantoni, and M. J. Perry, "Underwater gliders for ocean research," *Mar. Technol. Soc. J.*, vol. 34, pp. 48–59, 2004.
- [2] D. C. Webb, "SOFAR floats for POLYMODE," in *Proc. OCEANS Conf.*, Los Angeles, CA, 1977, pp. 44B-1–44B-5.
- [3] R. E. Davis, D. C. Webb, L. A. Regier, and J. Dafour, "The autonomous Lagrangian circulation explorer (ALACE)," *J. Atmos. Ocean. Technol.*, vol. 9, pp. 264–285, 1992.
- [4] D. C. Webb, P. J. Simonetti, and C. P. Jones, "SLOCUM: An underwater glider propelled by environmental energy," *IEEE J. Ocean. Eng.*, vol. 26, no. 4, pp. 447–452, Oct. 2001.
- [5] S. Wang, C. Xie, Y. Wang, L. Zhang, W. Jie, and S. J. Hu, "Harvesting of PEM fuel cell heat energy for a thermal engine in an underwater glider," *J. Power Sources*, vol. 169, pp. 338–346, 2007.
- [6] L. Muscatine, L. R. McCloskey, and R. E. Marian, "Estimating the daily contribution of carbon from zooxanthellae to coral animal respiration," *Limnology Oceanogr.*, vol. 26, pp. 601–611, 1981.
- [7] P. Kremer, J. Costello, J. Kramer, and M. Canino, "Significance of photosynthetic endosymbionts to the carbon budget of the scyphomedusa *Linuche unguiculata*," *Limnology Oceanogr.*, vol. 35, pp. 609–624, 1990.
- [8] D. T. Welch, R. J. K. Dunn, and T. Meziane, "Oxygen and nutrient dynamics of the upside down jellyfish (*Cassiopea sp.*) and its influence on benthic nutrient exchanges and primary production," *Hydrobiologia*, vol. 635, pp. 351–362, 2009.
- [9] A. Villanueva, S. Bresser, S. Chung, Y. Tadesse, and S. Priya, "Jellyfish inspired underwater unmanned vehicle," *Proc. SPIE—Int. Soc. Opt. Eng.*, vol. 7287, DOI:10.1117/12.815754, 72871G.
- [10] S. P. Colin and J. H. Costello, "Morphology, swimming performance and propulsive mode of six co-occurring hydromedusae," *J. Exp. Biol.*, vol. 205, pp. 427–437, 2002.
- [11] A. A. Villanueva, K. B. Joshi, J. B. Blottman, and S. Priya, "A bio-inspired shape memory alloy composite (BISMAC) actuator," *Smart Mater. Struct.*, vol. 19, 2010, DOI: 10.1088/0964-1726/19/2/025013, 025013.
- [12] J. V. Dave, "Performance of a tilted solar cell under various atmospheric conditions," *Solar Energy*, vol. 21, pp. 263–271, 1978.
- [13] M. C. Gonzalez and J. J. Carrol, "Solar cells efficiency variations with varying atmospheric conditions," *Solar Energy*, vol. 53, pp. 395–402, 1994.
- [14] M. C. Stoddard and F. P. Incropera, "Distribution of solar radiation in natural waters under field conditions," *Solar Energy*, vol. 28, pp. 425–432, 1982.
- [15] J. A. Muaddi and M. A. Jamal, "Spectral response and efficiency of a silicon solar cell below water surface," *Solar Energy*, vol. 49, pp. 29–33, 1992.
- [16] J. Wang and J. Seyed-Yagoobi, "Effects of water turbidity and salt concentration levels on penetration of solar radiation under water," *Solar Energy*, vol. 52, pp. 429–438, 1994.
- [17] R. Gottschalg, D. G. Infield, and M. J. Kearney, "Experimental study of variations of the solar spectrum of relevance to thin film solar cells," *Solar Energy Mater. Solar Cells*, vol. 79, pp. 527–537, 2003.
- [18] J. Y. Chen and K. W. Sun, "Enhancement of the light conversion efficiency of silicon solar cells by using nanoimprint anti-reflection layer," *Solar Energy Mater. Solar Cells*, vol. 94, pp. 629–633, 2010.
- [19] C. Strümpel, M. McCann, G. Beaucarne, V. Arkhipov, A. Slaoui, V. Svrcek, C. del Cañizo, and I. Tobias, "Modifying the solar spectrum to enhance silicon solar cell efficiency—An overview of available materials," *Solar Energy Mater. Solar Cells*, vol. 91, pp. 238–249, 2007.
- [20] E. Custodio, L. Acosta, P. J. Sebastian, and J. Campos, "A better solar module performance obtained by employing an infrared water filter," *Solar Energy Mater. Solar Cells*, vol. 70, pp. 395–399, 2001.
- [21] D. Yun, W. Feng, H. Wu, and K. Yoshino, "Efficient conjugated polymer-ZnSe and -PbSe nanocrystals hybrid photovoltaic cells through full solar spectrum utilization," *Solar Energy Mater. Solar Cells*, vol. 93, pp. 1208–1213, 2009.
- [22] PowerFilm Solar, [Online]. Available: <http://www.powerfilmsolar.com>
- [23] Apogee, [Online]. Available: <http://www.apogeeinstruments.com>
- [24] Hamilton Technology, [Online]. Available: <http://www.hamiltontechnology.com>
- [25] Advanced Aquarist, [Online]. Available: <http://www.advancedaquarist.com/issues/july2004/review.htm>

- [26] J. O. Dabiri, S. P. Colin, J. H. Costello, and M. Gharib, "Flow patterns generated by oblate medusan jellyfish: Field measurements and laboratory analyses," *J. Exp. Biol.*, vol. 208, pp. 1257–1265, 2005.
- [27] W. G. Gladfelter, "Structure and function of the locomotory system of the Scyphomedusa cyanea capillata," *Mar. Biol.*, vol. 14, pp. 150–160, 1973.



Keyur B. Joshi received the B.S. degree in mechanical engineering from The Maharaja Sayajirao University of Baroda, Gujarat, India, in 2001 and the M.Tech. degree with design specialization from Indian Institute of Technology—Bombay, India, in 2006. Currently, he is working towards the Ph.D. degree at the Department of Mechanical Engineering, Virginia Tech, Blacksburg.

He received ISRO Fellowship during his M.Tech. and developed novel model on "slosh dynamics" and strategies for slosh cancellation. After graduation, he worked with GE Healthcare as Software Design Engineer and later with GE Aviation as Analysis Engineer in Large Commercial Aircraft Engine Structure group. He achieved "hats off" award for his work on failure investigation and fatigue life estimation on one of the failing component that could not be monitored in the field. Mr. Joshi also earned "Six Sigma Green Belt" during his service at GE Aviation. He has authored around six journal publications.



John H. Costello received the B.S. degree from Williams College, Williamstown, MA, in 1981, the M.S. degree from the University of South Carolina, Columbia, in 1987, and the Ph.D. degree in biology from the University of Southern California, Los Angeles, in 1987.

He is currently a Professor in the Biology Department, Providence College, Providence, RI and an Adjunct Research Scientist at the Marine Biology Laboratory, Woods Hole, MA. He specializes in the study of gelatinous zooplankton behavior and biomechanics and he has authored over 65 publications in this area.



Shashank Priya received the integrated M.E. degree from Indian Institute of Science, Bangalore, India, in 2000 and the Ph.D. degree in materials engineering from Pennsylvania State University, Philadelphia, in 2002.

He is currently an Associate Professor in the Department of Materials Science and Engineering and the Department of Mechanical Engineering, Virginia Tech, Blacksburg. He is also serving as the Associate Director of the Center for Intelligent Material Systems and Structures (CIMSS) and the Director of NSF I/UCRC: Center for Energy Harvesting Materials and Systems (CEHMS). Prior to joining Virginia Tech, he was an Assistant Professor at the Department of Materials Science and Engineering at The University of Texas Arlington. He has worked at several prestigious companies including Murata Manufacturing Ltd., Shiga, Japan, and APC International, PA. He is one of the pioneers in the area of energy harvesting, and laminate magnetoelectric composites. He has authored over 155 publications in international journals and four patents.

Dr. Priya has received several awards including: the 2011 Deans Research Excellence Award presented by Virginia Tech; the 2007 Nominee for "Outstanding Technology of the Year Award" presented by the International Academy of Science, Independence, MO; the 2006 Research Excellence Award presented by The University of Texas Arlington; the 2005 Automation and Robotics Research Institute Outstanding Researcher Award presented by The University of Texas Arlington; the 2004 Dr. R. L. Thakur Memorial Award presented by the Indian Ceramic Society; the 2002 Metals, Materials and Metallurgical Transactions Society (TMS) Shri Ram Arora International Award; the 1999–2000 VidyaBharti, Indian Institute of Metals (IIM) gold medal; and the 1999–2000 K. K. Mallik Gold Medal of the Indian Institute of Science, India.